Simultaneous Observation of Phase-Stepped Images for Photoelasticity Using Diffraction Gratings

S.L.B. Kramer · B.A. Beiermann · S.R. White · N.R. Sottos

Abstract Phase-stepped photoelasticity is a powerful method for full-field stress analysis, but sequential collection of the multiple required images limits the technique to static loading applications. We have developed a system that utilizes diffraction gratings to collect four phase-stepped images simultaneously with a single camera for transient loading applications. Two adjacent, perpendicularly oriented, 1D Ronchi rulings are placed after a transparent sample to split the light into equal intensity beams for each diffraction order. The four beams that are diffracted once in the x direction and once in the y direction transmit through arrays of analyzing polariscope elements, with different combinations of fast-axis orientations for four phase-stepped images. The mirrors and imaging lenses in the system work in concert to focus each beam onto separate quadrants of the same CCD. We demonstrate the system for stress analysis of compressive loading of a Homalite-100 disk and of a Homalite-100 plate with a central hole. This system has the potential for photoelastic analysis of time-dependent materials and of dynamic events, when equipped with a high-speed camera.

Keywords Photoelasticity · Phase-stepping · Diffraction grating · Stress analysis · Single camera

S.L.B. Kramer (SEM Member) (✉) · B.A. Beiermann · S.R. White (SEM Member) · N.R. Sottos (SEM Member)
University of Illinois at Urbana-Champaign, 405 N Mathews Ave., Urbana, IL 68122, USA
e-mail: slkrame@sandia.gov

Present Address:
S.L.B. Kramer (SEM Member)
Sandia National Laboratories, 1515 Eubank Ave. SE, Albuquerque, NM 87123, USA

Introduction

Photoelasticity is an optical stress analysis method that can be performed in transmission or in reflection to determine the difference in principal stresses or strains in the deformed medium, respectively. Polarized light passes through a stress-birefringent material, which acts as a temporary linear retarder plate with retardation δ at orientation of θ, and is then analyzed with polarizing elements. The resulting interference pattern is related to both the direction of the principal axes with respect to a reference axis (isoclinic angle, θ) and the stress/strain state (isochromatic phase, δ). Varying the orientation of the polarizing optics for the same state of deformation results in different interference patterns. Phase-stepping photoelasticity is a technique where combinations of different interference patterns are specifically chosen as to isolate θ and δ through trigonometric equations.

Full-field imaging with phase stepping allows for the determination of θ and δ over an entire field of view as opposed to a single point. Phase-stepped images are taken either sequentially, by rotating the polarizing elements and imaging with one camera, or simultaneously, by splitting the polarized light after the specimen, sending the split light through different analyzing optics, and imaging with one or multiple cameras [1–7]. Sequential image capture does not allow for stress analysis of time-dependent deformation states. Simultaneous image capture with several cameras is not practical from the standpoint of camera cost (particularly high-speed cameras), physical space occupied by each camera, and image-capture synchronization. Hobbs et al. [7] developed an instrument for phase-stepped photoelasticity with simultaneous image capture with one camera, featuring a series of beam-splitters and prisms to redirect four phase-

stepped images to one camera. One of the limitations of this instrument was the sodium lamp light source, which had to be intense and stable due to beam splitting and high-rate image capture. Additionally, the instrument had a limited field of view due to the imaging optics. Yoneyama and co-authors [4, 5] developed a single-camera method where the analyzing polariscope optics are arranged in arrays of 2 x 2 pixels that directly overlay the CCD sensor, and the images are post-processed by dividing the pixelated data into four phase-stepped images. This method is not practical for most researchers because the microarray of polarizing elements is a custom optical component.

Here, we introduce an alternative approach to simultaneous capture of phase-stepped photoelastic images with one camera that utilizes a monochromatic laser beam light source, transmission diffraction gratings for beam splitting, and mirrors and lenses for beam redirection and imaging. The first study using beam-splitting transmission diffraction gratings for simultaneous capture of four images with one camera was for diffraction-grating holography, a wavefront curvature measurement technique [8]. This technique requires custom diffraction gratings tuned for the each particular CCD to produce properly spaced images that do not overlap and fit on the single CCD. In contrast, our method utilizes off-the-shelf components and is highly configurable, allowing for a wide range of light intensities and wavelengths, different camera formats, and a wide range of field of view sizes. Our study is the only other application of a diffraction-grating beam-splitting method for

single-camera phase-stepped interferometry, and thus, the first for photoelasticity. In this paper, we outline the system components and the design approach, demonstrate the technique for phase-stepped photoelastic images of two cases, a compressed Homalite-100 disk and a compressed Homalite-100 plate with a central hole, characterize potential error sources, and discuss the potential applications of this new approach.

Design

The guiding principles for our simultaneous capture of four phase-stepped images are the following:

1. to have the same field intensity, I_o, for each image,
2. to separate the beams so that each can go through different analyzing polariscope optics,
3. to maximize the pixels used on the single camera sensor without overlapping the images, and
4. to minimize image distortions introduced by beam-directing and imaging optics.

Figure 1 depicts the basic elements of the experimental setup for two of the beams I_3 and I_4; the other two beams I_1 and I_2 (not shown) are mirrored across the y-z plane, each with its own set of optics. The circular polariscope consists of a monochromatic coherent laser with beam expansion and collimation capabilities; the initial polarizer P and quarter-wave plate Q; the deformed specimen, here a
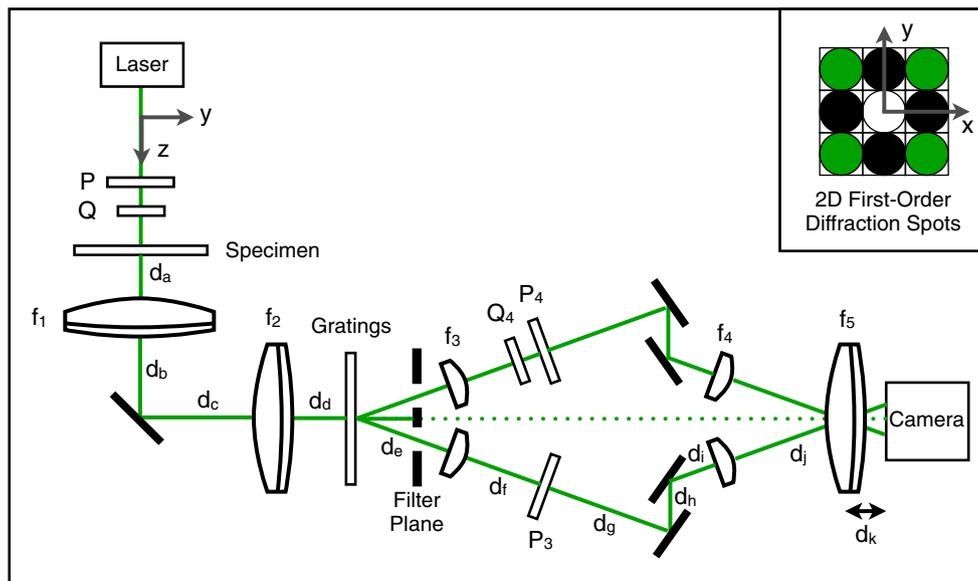
Fig. 1 Design of optical setup: monochromatic light is split using 2D diffraction, and ($\pm 1, \pm 1$) beams, shown as the four lighter color (green online) corner first-order diffraction spots in the inset, are selected and redirected to a single camera. The two split beams shown here for I_3 and I_4 mirror each other across the x-z plane. The beams for I_1 and I_2, not shown here, mirror the beams for I_3 and I_4 across the y-z plane and have identical optics with different orientations of the analyzing polariscope optics. The z-axis follows the (0,0) beam path by convention, and the coordinate system reflects at 45° with the beam after the turning mirror before lens f_2

transparent photoelastic material; and analyzing polariscope elements Q_i and P_i for each of the four beams. The other optics not used in the polariscope have several purposes:

1. a 45° turning mirror and lenses f_1 and f_2 for beam redirection away from the load frame, for beam relaying, and for beam reduction; transmission diffraction grating(s) for 2D beam splitting,
2. a filter plane to block the unwanted diffraction orders,
3. lenses f_3 and f_4 for beam relaying,
4. two mirrors per beam for redirection towards the camera,
5. an imaging lens f_5 and a single camera.

The distances d_i and focal lengths of the lenses f_i depend on the camera sensor size, the desired field of view, and the available space after the specimen.

The polarization optics for the circular polariscope depend on the choice of phase-stepping method. The orientation of optics and resulting four phase-stepped images for this study are given in Table 1. Inspired by the phase-stepping from Hobbs et al. [7] and the trigonometric functions from Ajovalasit et al. [9], the isoclinic angle and isochromatic phase are determined using

$$
\begin{aligned}
\theta &= \frac{1}{2}\arctan\left(\frac{I_2 - I_3}{I_2 + I_3 - 2I_1}\right) \\
&= \frac{1}{2}\arctan\left(\frac{\sin(2\theta)\sin(\delta)}{\cos(2\theta)\sin(\delta)}\right) \text{ for } \sin(\delta) \neq 0,
\end{aligned} \tag{1}
$$

$$
\begin{aligned}
\delta &= \arctan\left(\frac{I_2 + I_3 - 2I_1}{\cos(2\theta)\left(2I_4 - (I_2 + I_3)\right)}\right) \\
&= \arctan\left(\frac{\cos(2\theta)\sin(\delta)}{\cos(2\theta)\cos(\delta)}\right) \text{ for large values of } \cos(2\theta),
\end{aligned} \tag{2}
$$

Table 1 Orientations of the quarter-wave plate and analyzing linear polarizers and image intensities for the four phase-stepped images

Image	Quarter-plate angle	Analyzing polarizer angle	Intensity
I_1	None	$\pi/2$	$I_o[1 - \sin(\delta)\cos(2\theta)]$
I_2	None	$3\pi/4$	$I_o[1 + \sin(\delta)\sin(2\theta)]$
I_3	None	0	$I_o[1 - \sin(\delta)\sin(2\theta)]$
I_4	$3\pi/4$	0	$I_o[1 + \cos(\delta)]$

The angles are relative to the axis perpendicular to the loading direction of a uni-axial load frame. The input polarizer and quarter-wave plate before the specimen are at $\pi/2$ and $3\pi/4$, respectively

and

$$
\begin{aligned}
\delta &= \arctan\left(\frac{I_2 - I_3}{\sin(2\theta)\left(2I_4 - (I_2 + I_3)\right)}\right) \\
&= \arctan\left(\frac{\sin(2\theta)\sin(\delta)}{\sin(2\theta)\cos(\delta)}\right) \text{ for large values of } \sin(2\theta).
\end{aligned} \tag{3}
$$

The design for the setup began with the choice of beam splitting. Inspired by the Coherent Gradient Sensing interferometry technique that utilizes Ronchi ruling gratings for wavefront shearing [6, 10], we split a monochromatic laser beam with diffraction gratings in 2D. We then select four beams that have undergone the same path length with the same diffraction orders (and thus equivalent intensity) by blocking other beams. The inset of Fig. 1 depicts the 2D first-order diffractions spots, which have two sets of four equal intensity beams. The black spots represent the $(\pm1,0)$ and $(0,\pm1)$ beams, which are diffracted once in the x or the y direction, and the lighter spots (green online) represent the $(\pm1,\pm1)$ beams, which are diffracted once both in the x and the y direction. These diffraction orders are obtained either by a single 2D diffraction grating with pitch (line spacing), p, in both directions or by two adjacent 1D diffraction gratings with pitch p and with the two gratings oriented perpendicularly. The angle of diffraction, κ, which is the angle at which the diffracted beam propagates away from the incident beam, is given by $\kappa = \sin^{-1}[m\lambda/p]$, where m is the diffraction order and λ is the wavelength of light. The light will continue to propagate in space at this angle unless manipulated by other optics after the grating. Given that a camera sensor is generally rectangular, a practical choice to best fill the sensor area with the four beams is the corner $(\pm1,\pm1)$ beams. These beams travel at an angle $\pm\kappa$ relative to both the x- and y-axes, and therefore, the downstream optics are in square arrays with each optic centered at a corner of an array. The angle κ must be sufficiently large to allow for enough beam separation without requiring prohibitively large distances d_i and for the beams to pass through the center of their downstream optics to minimize image distortion.

The interference pattern formed by a beam passing through the analyzing optics is a function of the polarization state of the beam prior to entering the analyzing optics and of the orientation of the analyzing optics, as given in Table 1. To reliably interpret the interference pattern in terms of θ and δ, we must ensure that the polarization state of the beam prior to the analyzing optics is only due to the initial polarization optics and the deformation in the specimen. In general, changes to polarization after the analyzing optics does not affect the interference pattern, so optics that affect polarization may be used after the analyzing optics. Diffraction through a transmission line grating with pitch p greater than light wavelength λ does not lead to changes

in light polarization along the beam path, so the diffraction gratings may be placed before the analyzing optics for the beam splitting. Reflection off a 45° mirror only results in a reflection of the y-axis about the x-axis without changing the polarization state relative to the optical axis. Therefore, a 45° turning mirror after lens f_1 does not affect the resulting interference pattern, assuming that the reflection of the optic axis is correctly accounted for in the orientation of the analyzing optics. In contrast, reflections off mirrors at angles other than 45° can lead to changes in light polarization relative to the optical axis. The non-45° mirrors that redirect the beams towards the camera are placed after the analyzing optics.

Another key design feature is the combination of imaging lens f_5 and angle β of the beams after the redirecting mirrors. The imaging lens is placed a distance $d_k = f_5$ from the camera sensor (i.e. focused at infinity) so that the location of the beams on the sensor is based on the angle of the light. In this configuration, a beam with angle $\pm\beta$ relative to the z-axis along both x- and y-axes will be focused to an (x_{sensor}, y_{sensor}) location of ($\pm\beta \times f_5$, $\pm\beta \times f_5$). This method allows for precise placement of the images on the camera sensor with good image separation. Additionally, to reduce potential distortions from the imaging lens, the four beams transmit through the center of the imaging lens at their respective angles $\pm\beta$. In other words, the beams cross at the center of the imaging lens, as shown in Fig. 1, by careful choice of the distance traveled from the mirrors to the camera, ($d_i + d_j$), and of the distance of the mirrors from the centerline.

Given the choices of laser wavelength, diffraction grating pitch, camera, angle β for the redirected beams, and imaging lens f_5, the design of the remaining lenses f_1 through f_4 and distances d_a through d_i is an optimization problem based on the physical constraints of the setup (table length, size of available optics, and mounting options for optics) and the desired field of view. As summarized in the Appendix, we performed this optimization through Fourier wave-optics analysis of the optical system in order to obtain focused images of the four beams with the desired field of view. We found from this analysis that if lenses f_1 and f_2 are located at the sum of their focal lengths apart (resulting in a collimated beam after lens f_2), then the distance d_j between lenses f_4 and f_5 does not affect the focus or the magnification of the final image. This finding implies that distance d_j can easily be chosen to optimize the location of the four beams on the camera sensor.

Experimental Setup

The experimental setup for this study includes the following components and placement. The light source is

a single longitudinal mode diode-pumped green 532-nm wavelength laser (model CrystaLaser CL532-025S). The beam is expanded from a 0.36-mm diameter slightly divergent beam to an approximately 12-mm diameter collimated beam using a spatial filter for the Newport Corporation and 200-mm focal length, 25.4-mm diameter, achromatic doublet collimating lens from Thor Labs. The power of the polarized laser is controlled using a combination of a half-wave plate and polarizer before the first two polarizing elements of the circular polariscope.

All 15-mm diameter clear-aperture zero-order quartz wave plates are from Edmund Optics and are matched for the 532-nm wavelength. The 25.4-mm diameter sheet linear polarizers are from New Focus. Lenses f_1 and f_2 are 50.8-mm diameter achromatic doublets with focal lengths 200 mm and 75 mm from Thor Labs, with larger radius side facing towards the specimen. Lenses f_3 and f_4 are 25.4-mm diameter plano-convex lenses with the same 125-mm focal length from Thor Labs.

The diffraction gratings are two adjacent 1D Ronchi ruling transmission gratings, chrome on glass from Applied Image, oriented with the lines perpendicularly, with pitch p of (1/150) mm (6.67 μm). The resulting first-order diffraction angle κ for 532-nm light is 0.0799 radians (4.58^o). The turning mirror between lenses f_1 and f_2 is 38 mm × 25 mm and is oriented at 45° relative to the incoming beam. The redirecting mirrors have a 25.4-mm diameter. The imaging lens f_5 is a Nikon Micro-Nikkor 60-mm f/2.8D lens, with its focus set at infinity (distance d_k of 60 mm) and with its largest aperture size. The front of the lens (approximately 22-mm in diameter) acted as an aperture for each beam, setting the size of the images on the camera sensor. The camera is a Stingray F504B CCD with a 2452 pixel × 2056 pixel sensor with 3.45 μm × 3.45 μm pixel size, meaning an 8.46 mm × 7.09 mm sensor.

The angle β for the beams after the second redirecting mirror is 0.03 radians (1.72^o), resulting in a placement of each beam (±1.8 mm, ±1.8 mm) from the center of the camera sensor, or 25.4 % of the shorter sensor length away from the center in both x and y. The four beams are well separated into each quadrant of the sensor. Based on the Fourier analysis of the actual thick lenses, distances d_a through d_k are listed as the distance from the back surface of an optic to the front of the next optic: 50 mm, 148 mm, 120 mm, 35 mm, 221 mm, 150 mm, 242 mm, 42 mm, 118 mm, 522 mm, and 60 mm. This alignment leads to a pixel to specimen length ratio of 130.5 pixels/mm. Thus, the maximum visible length on the specimen that can fit on the camera sensor without the images overlapping is around 7.8 mm. Slight adjustments in the location of lenses f_3 and f_4 allow pixel to specimen length ratio of 120–150 pixels/mm, meaning a maximum visible length on the specimen of 8.5

mm down to 6.8 mm for this set of optics. The image resolution of this system is 24.8 μm (1951 USAF resolution target Group 4, Element 3), which implies that the smallest object that the CCD with 3.45-μm pixels at a magnification of -0.45 around 7-8 pixels. Thus, the resolution is limited by the lenses, not by the CCD sensor size.

Demonstration of the Technique

Compressed Disk

We utilized the experimental setup described above to analyze the stresses in a disk subjected to diametric compression, a classical problem with a well-known analytical solution. The 5.57-mm diameter disk was cut from a sheet of Homalite-100 with 1.39-mm thickness. The disk was compressed in a uni-axial load frame, oriented in the y-axis direction of the optics. Figure 2(a) shows the experimental image of the four phase-stepped photoelastic patterns for a compressive load of 49 N, and Fig. 2(b) shows the corresponding theoretical image for this configuration. The fringe patterns in the experimental image compare well with those in the theoretical image; a Gaussian non-uniform laser beam light source results in a smaller intensity $I_o(x, y)$ near the edges of the disk in the experimental images, an effect replicated in the theoretical patterns using a range of $0.18 I_o^{max}$ to I_o^{max}.

The four patterns are separated and collocated in order to evaluate θ and δ over the entire disk. Equation (1) results in a wrapped isoclinic angle with range $(-\pi/4, \pi/4]$, as shown in Fig. 3(a)–(b), so we unwrapped the field to represent the full range of the data. We employed a quality-based unwrapping algorithm written in MATLAB similar to the program from Siegmann et al. [11], where positive and negative regions are identified and then compared using the highest quality pixel on the boundaries of these positive and negative regions. We first performed a Weiner filter (with a 50 pixel × 50 pixel window) to reduce local noise, and then unwrapped adjacent positive and negative regions with large areas (greater than 100 pixels) using the highest quality pixels on their long boundaries. We finally unwrapped the smaller regions. The regions outside the disk and the slight caustic shadows near the load application points were masked to prevent unwrapping errors. The quality map, described by Kramer et al. [6], is based on giving high quality values to pixels with either small differences with their neighbors, implying continuity, or large differences close to the wrapped phase jump of $\pi/2$, implying a need to unwrap that region. The unwrapped isoclinic angle maps from the experiment and theory in Fig. 3(c)–(d) show good global agreement. The main differences between these fields are in regions where $\sin(\delta)$ is close to 0 (i.e. division of two small numbers in equation (1) that do not perfectly cancel in experimental data as will be discussed later.) The global root-mean-squared (rms) error averaged over the entire field is 0.083 radians (4.7^o), which is a small normalized rms error of 1.8 % of the observed data range.

With the unwrapped isoclinic angle and the four images, we used equations (2) and (3) to obtain the wrapped isochromatic phase, as shown in Fig. 3(e)–(f), and then employed the same algorithm for phase unwrapping as the isoclinic angle, but using a phase jump of π. Figure 3(g)–(h) are the unwrapped isochromatic phase maps from the experiment and theory. These fields have an rms error of 0.25 radians, which translates to 0.53 MPa, and a normalized rms error of 2.1 %. Here, much of the error comes from near the

Fig. 2 Image from a single camera with the four phase-stepped photoelastic patterns (I_1 upper left; I_2 lower left; I_3 upper right; and I_4 lower right) for a compressed Homalite-100 disk with 5.57-mm diameter and 1.39-mm thickness with the loading direction along the long axis of the image (y-axis): (**a**) Experimental image for a compressive load of 49 N; (**b**) Theoretical image for a compressive load of 49 N from a Gaussian intensity light source

1.5 mm

1.5 mm

(a) **(b)**
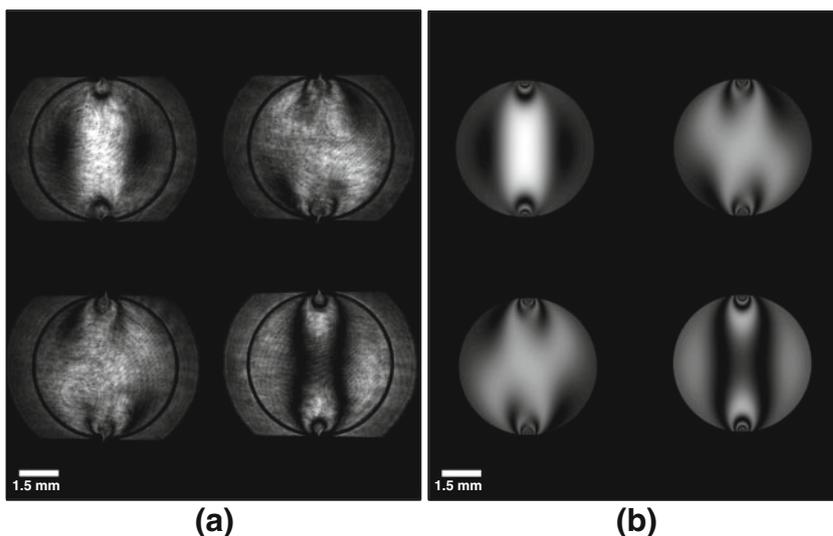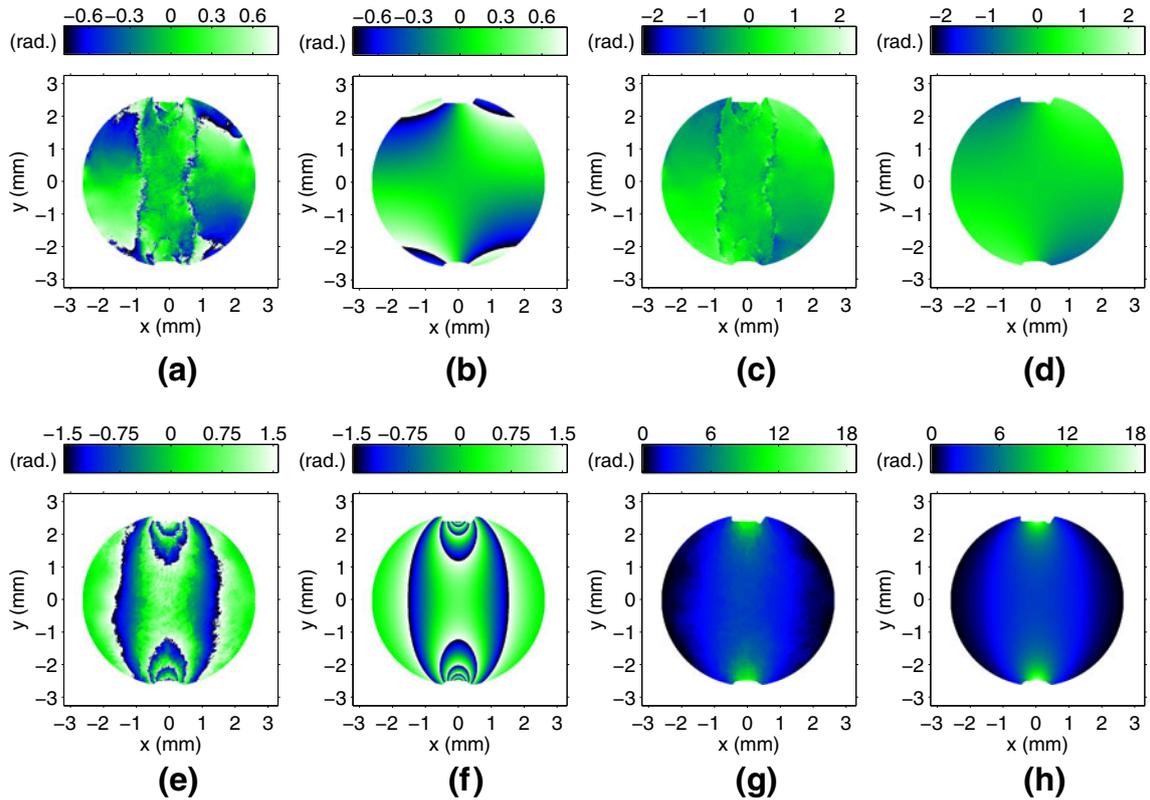
Fig. 3 Wrapped and unwrapped isoclinic angle and isochromatic phase maps with the load along the vertical *y*-axis and with a white mask around the disk and close to the points of load application where there are slight caustic shadows: (**a**) experimental wrapped isoclinic angle, (**b**) theoretical wrapped isoclinic angle, (**c**) experimental unwrapped isoclinic angle, (**d**) theoretical unwrapped isoclinic angle, (**e**) experimental wrapped isochromatic phase, (**f**) theoretical wrapped isochromatic phase, (**g**) experimental unwrapped isochromatic phase, and (**h**) theoretical unwrapped isochromatic phase. (Color online)

load application points, where the experimental images do not reach the expected theoretical values due to the image resolution in this setup.

Figure 4(a)–(b) are the experimental and theoretical θ and δ along the $y = -R/2$ line. The experimental isoclinic angle has some discontinuities due to error sources such as the image noise and the discrete image intensity values, which will be discussed later. These discontinuities are similar to those found in other experimental isoclinic angle fields from digital photoelasticity [4–6, 11]. The isochromatic phase along $y = -R/2$ qualitatively has similar comparison between the experimental and theoretical values as Yoneyama et al. [5] and Hobbs et al. [7]. Table 2 provides the rms and normalized rms error for five different loads on the disk. The compressive load platen on a spherical ball was slightly off-parallel with the fixed load platen for the

Fig. 4 Unwrapped experimental data (*red circles*) compared to theoretical values (*blue line*) along the $y = -R/2$ line for a compressive load of 49 N: (**a**) isoclinic angle in radians, (**b**) isochromatic phase in radians. (Color online)
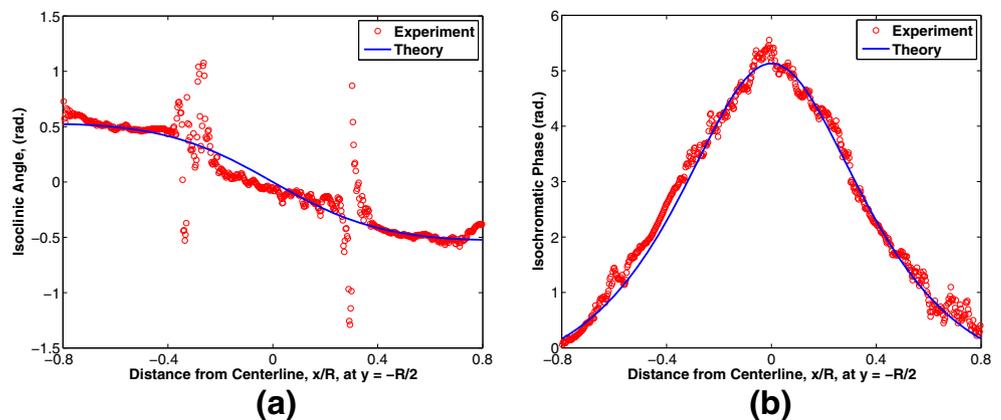
Table 2 Experimental rms error and normalized rms error for five loads applied to the Homalite-100 disk

Applied load (N)	θ rms (rad.)	θ nrms (%)	δ rms (rad.)	δ rms (MPa)	δ nrms (%)
5	0.291	4.1	0.15	0.32	3.4
16	0.161	2.8	0.19	0.40	2.8
27	0.083	1.8	0.14	0.29	1.4
38	0.080	1.4	0.23	0.48	2.0
49	0.083	1.8	0.25	0.52	2.1

first two loads at 5-N and 16-N, leading to a loading condition different than theory, hence larger errors, particularly in the isoclinic angle. For the three high loads, the isoclinic angle has a more steady state error, while the error in the isochromatic phase appears to be increasing. This increasing error in δ may be due to imperfect point load application and due to the image resolution being too coarse to resolve the dense fringes at the load application, as seen in Fig. 2. The normalized rms errors for all fields at all of these loads are less than 5 %. Therefore, this example of stress analysis of a diametrically compressed disk demonstrates that this technique overall gives quality phase-stepped photoelastic data obtained simultaneously with a single camera.

Compressed Plate with a Central Hole

The following example is a uniform compressive load on the sides of small Homalite-100 plate with a central hole, as shown in Fig. 5(a). We used the same experimental setup as described for the compressed disk above. Figure 5(b) is an image with a single CCD for a 12.60 mm × 12.64 mm Homalite-100 plate with a 1.63-mm diameter central hole and 1.50-mm thickness with a compressive load of 199 N. Images I_2 and I_3 in the upper right and lower left corners have the opposite intensities, as expected from their intensities in Table 1. Image I_4 is symmetric about the x- and y-axes, as expected for the symmetric stress state for this loading condition. The image of each beam is approximately a 7.3-mm diameter circle corresponding to the portion of the beam that was able to transmit through the 22-mm diameter imaging lens f_5. We chose a 4.40 mm x 4.40 mm square area centered on the hole in the plate for the photoelastic analysis.

The collocated phase-stepped images were analyzed as described for the compressed disk. Figure 6 contains the unwrapped isoclinic angle and isochromatic phase maps for the central analysis region for the compressive load of 199 N. The isoclinic angle was successfully unwrapped (Fig. 6(a)), and is continuous except for the π jumps along a portion of the y-axis. By definition, the isoclinic angle is allowed to have phase jumps of π since θ indicates the

angle of the principal stress axes relative the chosen Cartesian coordinates. The corresponding isochromatic phase (Fig. 6(b)) is continuous and symmetric about the x- and y-axes, as expected from I_4. The isochromatic phase along the x-axis near the hole is approximately three times greater than that along the y-axis near the hole. This tripling of the stress is consistent with the stress concentration associated with a circular hole [12].

Discussion

Error Analysis and Setup Improvements

This first study of the diffraction-grating approach to simultaneous capture of phase-stepped photoelastic images demonstrates that the technique produces reasonable results, but with noticeable errors in the phase maps. Several error sources in this particular setup could be minimized to improve the results in future applications. These include the Gaussian laser beam intensity, random image noise, ring-like noise from back-reflections, influence of the quarter-wave plates, and coarse image resolution.

To investigate the effect of the Gaussian laser beam intensity, we modulated the theoretical intensity $I_o(x, y)$ with a 2D Gaussian profile similar to that of the experimental beam, where the range of intensity of $I_o^{Gaussian}$ on an 8-bit scale was 18-100 ($0.18 I_o^{max}$ to I_o^{max}.) The modulated theoretical images are given in Fig. 2(b). Additionally, we applied a random Gaussian image noise, standard deviation of 2 and range of ±15. Figure 7 overlays four image intensities for the $I_4 = I_o(x, 0)[1 + \cos(\delta)]$ for $y = 0$ for the compressive load of 49 N applied to the Homalite-100 disk: the unfiltered experimental intensity, the simulated intensity for a uniform laser beam intensity $I_o(x, y) = 100$, the simulated intensity for the Gaussian laser beam intensity $I_o^{Gaussian}$, and the simulated intensity for the Gaussian laser beam intensity $I_o^{Gaussian}$ with the random Gaussian noise. The general shape and intensity of the simulated Gaussian-modulated image is similar to that of the experiment. The Gaussian intensity causes a dramatic reduction in the intensity near the edges of the disk, as compared to theoretical intensity with a uniform input intensity. The random Gaussian noise is slightly smaller than the scatter of the experimental data at the edges of the disk, but similar in the center.

The random noise and ring-like noise result in pixelated wrapped isoclinic angle maps that are difficult to unwrap without propagating unwrapping errors. A common practice for reducing unwrapping errors due to image noise is to apply a local image filter, such as the Weiner filter that was used in this study, that reduces local noise while maintaining actual intensity variation due to the material stresses

Fig. 5 Compressed Homalite-100 12.60 mm × 12.64 mm plate with a 1.63-mm diameter central hole and 1.50-mm thickness: (**a**) schematic of loaded plate, indicating the 4.40 mm x 4.40 mm area analyzed, and (**b**) experimental image from a single camera with the four phase-stepped photoelastic patterns (I_1 upper left; I_2 lower left; I_3 upper right; and I_4 lower right) with the loading direction along the long axis of the image (*y*-axis) for a compressive load of 199 N

(a)

(b)
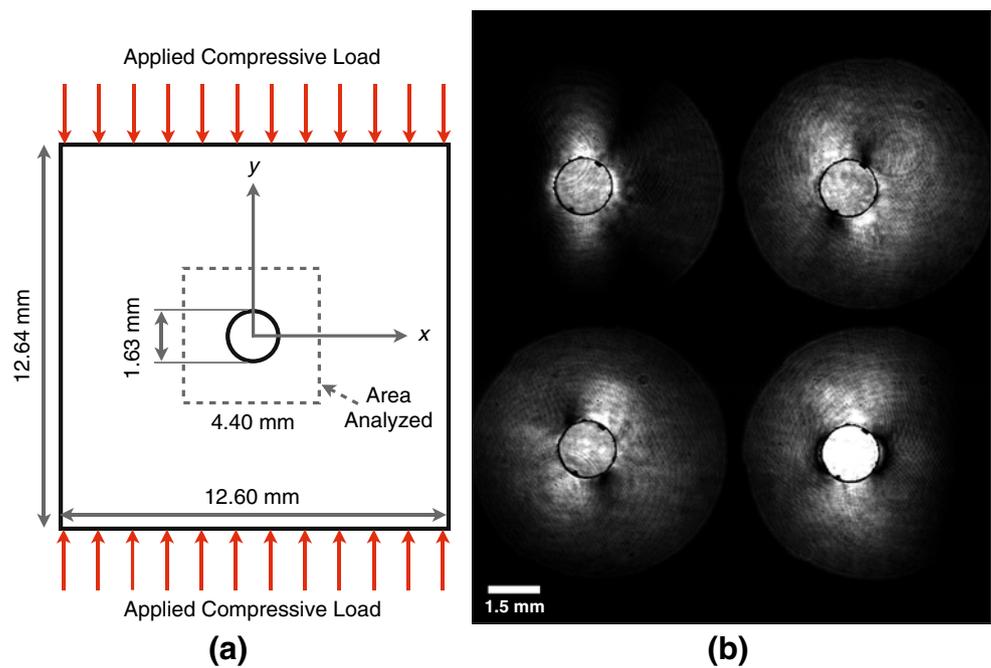
[6, 11]. This filtering process can lead to some errors in the phase maps, but makes unwrapping possible.

Figure 8(a)–(h) compares the wrapped isoclinic angle maps for the 49-N compressed Homalite-100 disk from experimental and simulated images with Gaussian laser beam intensity and / or random Gaussian noise and with or without Weiner image filtering. Additionally, Table 3 includes the global rms error of the wrapped isoclinic angle and wrapped ambiguous isochromatic phase, comparing each of these cases with the theoretical maps. The wrapped θ from the Gaussian beam theoretical images in Fig. 8(b) is nearly identical to the theoretical wrapped θ in Fig. 8(a) except where $\sin(\delta)$ approaches 0 (thin vertically oriented

peanut-shaped modulation) and around the $\pi/2$ phase jumps near the edges of the disk. These small modulations are because the discrete integer intensity values do not allow for analytically precise evaluation of the arctan() formula in equation (1). The wrapped phase maps from the simulated Gaussian intensity images have a small measurable global rms error. The images with random Gaussian noise lead to a wrapped θ in Fig. 8(e); both the $\pi/2$ phases jumps and the areas near where $\sin(\delta)$ approaches 0 are pixelated. The rms errors for both θ and δ are larger for the random Gaussian noise than for the Gaussian laser beam intensity.

The wrapped θ from the simulated images with the Gaussian laser beam intensity and the random Gaussian

Fig. 6 Unwrapped experimental data for the central 4.40 mm × 4.40 mm area of the compressed Homalite-100 plate with a central hole with the load along the vertical *y*-axis and with a white mask covering the central hole: (**a**) isoclinic angle map, which, by definition, is allowed phase jumps of π as those located along the *y*-axis, and (**b**) isochromatic phase. (Color online)

(a)

(b)
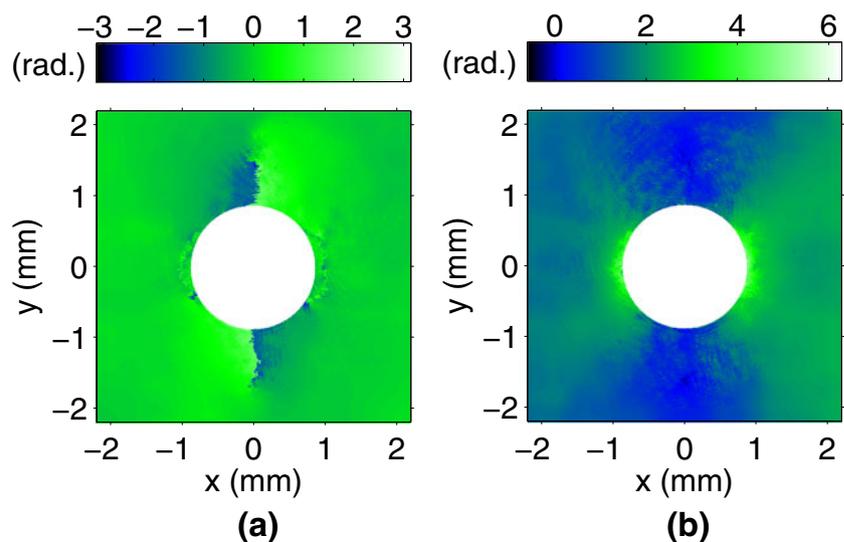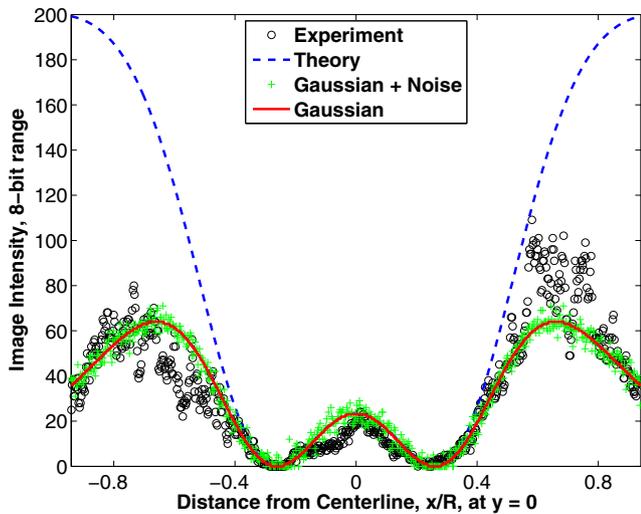
Fig. 7 Image $I_4 = I_o(x, 0)[1 + \cos(\delta)]$ for $y = 0$ for the compressive load of 49 N applied to the Homalite-100 disk, comparing the experimental intensity (*black circles*), the theoretical intensity with $I_o^{max} = 100$ (*blue dashed line*), the theoretical intensity with a Gaussian intensity $I_o^{Gaussian}$ ranging from 18-100 (*red solid line*), and the theoretical intensity with the Gaussian intensity and random noise (*green plus sign*). (Color online)

noise in Fig. 8(g) has even more pixelated values near the edges of the disk. This pixelation is because the random noise has a more significant effect where the input laser beam intensity values are lower, leading to greater rms error in θ and δ than for the individual error sources. The wrapped θ from the experiment in Fig. 8(c) and from the two simulated error sources in Fig. 8(g) have similar locations of pixelation near the edges and where $\sin(\delta)$ is close to 0. The experimental map does have a more grainy appearance because of the ring-like noise that was not simulated. The rms errors for the experimental wrapped θ and δ are higher than for the two simulated error sources because the experiments do have other error sources that were not simulated. This analysis demonstrates that a significant portion of the error in the experiments is due to the Gaussian laser beam intensity and random Gaussian noise that can come from CCD signal noise and dust on optics.

Filtering the images before evaluating the wrapped phase maps, though important to unwrapping, can both reduce and add to the error in the data, because in some places the pixelated noise is reduced, while regions with spatially dense intensity variation due to quickly changing θ and δ
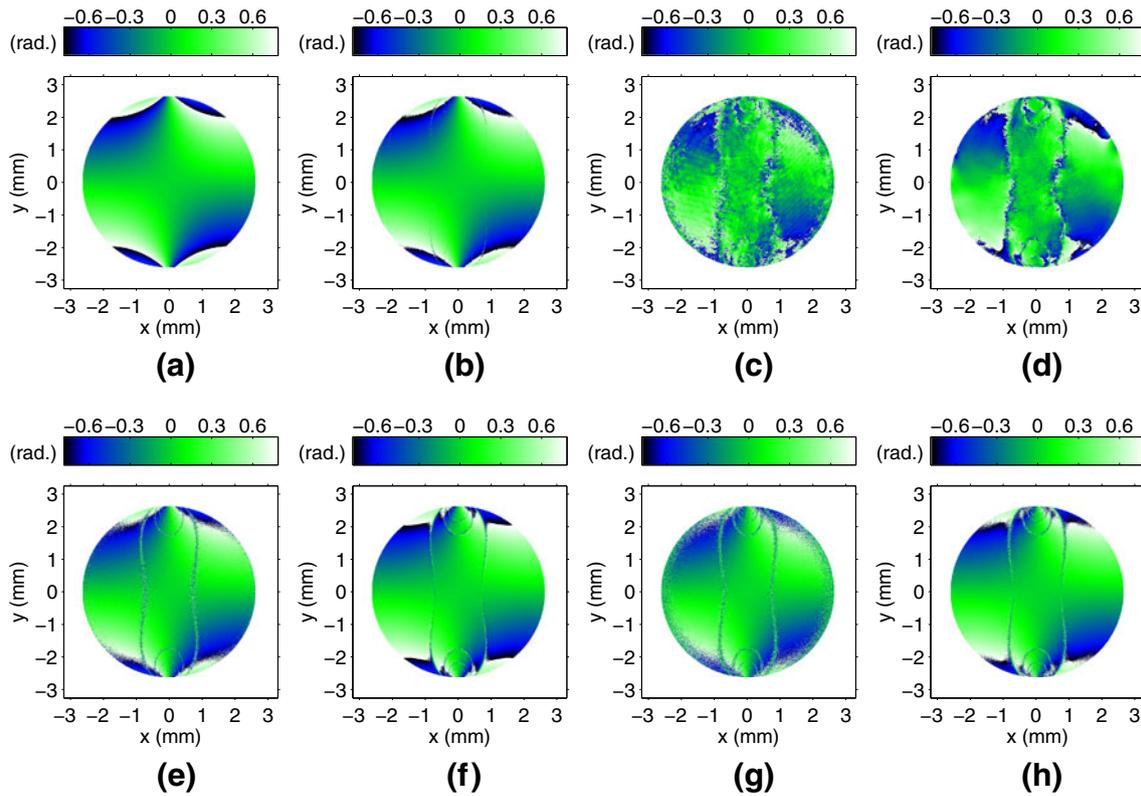
Fig. 8 Wrapped isoclinic angle maps from experimental and simulated images with different error sources and with or without image filtering for the compressive load of 49 N applied to the Homalite-100 disk: (**a**) theory (**b**) theory from images with Gaussian laser beam intensity, (**c**) experiment without image filtering, (**d**) experiment with image filtering, (**e**) theory from images with random noise, (**f**) theory from filtered images with random noise, (**g**) theory from images with Gaussian laser beam intensity and random noise, and (**h**) theory from filtered images with Gaussian laser beam intensity and random noise. (Color online)

Table 3 Comparison of rms error for wrapped θ and ambiguous wrapped δ for experimental data and simulated data that include different error sources for 49 N applied to the Homalite-100 disk

Data type	θ rms (rad.)	δ rms (rad.)	δ rms (MPa)
Experiment without filtering	0.169	0.26	0.54
Experiment with filtering	0.178	0.28	0.59
Gaussian beam	0.041	0.054	0.11
Random noise	0.061	0.092	0.19
Gaussian beam and random noise	0.109	0.110	0.23
Random noise with filtering	0.086	0.074	0.16
Gaussian beam and random noise with filtering	0.102	0.106	0.22

are blurred. The wrapped θ from filtered simulated images with random Gaussian noise in Fig. 8(f) has a smoother appearance, but errors were locally increased near the load application points where $\sin(\delta)$ is close to 0. The rms error for the wrapped θ increased for the filtered images with random noise as compared to the unfiltered images with random noise, but decreased for the wrapped δ. The wrapped θ from the filtered simulated images with Gaussian laser beam intensity and random noise again appears smoother, but with local errors still evident where $\sin(\delta)$ is close to 0. The global rms errors for θ and δ are about the same for the unfiltered and filtered simulated images with Gaussian laser beam intensity and random noise, but the wrapped phase maps from the filtered data could more easily be unwrapped. The wrapped θ from filtered experimental images in Fig. 8(d) has a less pixelated appearance as compared to the data from the unfiltered experimental images, allowing for unwrapping, but these fields have slightly higher rms error. Fortunately, the unwrapping process does reduce the rms errors in the filtered data, seen when comparing the values from Tables 2 and 3.

The additional error sources, which were not modeled, include the ring-like noise from back reflections, the influence of quarter-wave plates in polariscopes, and coarse image resolution. The circular white and dark fringes (ring-like noise) in Figs. 2(a) and 5(b) are due to back reflections off the final lens reflecting off the fourth set of lenses and then returning to the camera. This final lens in this setup was a Nikon macro lens that did not have an anti-reflective coating. Since the alignment of the beams throughout the optical system directly affects the placement of the beams on the CCD (related to angle of beam propagation and focal length of final lens), slight misalignments of lenses and

other optics that are usually acceptable to reduce interference from reflections are not easily tolerated in this setup. We did not explicitly add the ring-like back-reflection noise to the theoretical images for the error analysis since the range of modulation from this error source was similar to the random noise. The ring-like back reflections would add additional errors, likely on the same order of magnitude as the random Gaussian noise.

The error due to the quarter-wave plate in a polariscope has been an area of extensive research in photoelasticity [9, 13, 14]. In this particular setup, the input laser light and the quarter-wave plates were matched for 532-nm, reducing the error. Even with matched quarter-wave plates, the choice of angles of the polarizing optics for the photoelastic images can lead to small errors when calculating the isoclinic angle and isochromatic phase maps, particularly when only four images are used rather than six. Prashant and Ramesh [14] evaluated several combinations of photoelastic images for minimal quarter-wave plate influence; the authors selected an optimal four-image solution, from Ajovalasit et al. [9], that produced $I_o[1 \pm \cos(\delta)]$ and $I_o[1 \pm \sin(\delta)\sin(2\theta)]$ fields. We use a slightly different four-image solution, given in Table 1. Hence, there may be some small error due to the quarter-wave plates through this selection of four-image photoelasticity, but that error has not been characterized explicitly.

The image resolution in this setup is about 7-8 pixels, evident when comparing the high fringe density at the load application point of the experimental and theoretical images in Fig. 2 for the 49-N load on the Homalite-100 disk. The rms error increases due to larger error at the load application points as the load increases, showing that one significant error source, beyond those already discussed, is the coarse image resolution. The minimum resolvable fringe will be dictated either by the CCD pixel size or by the lenses; hence, this error source cannot be fully eliminated. The minimum resolvable fringe of any particular setup is an intrinsic limit on the capability.

The above error analysis elucidates the potential areas of improvement for the setup presented here. A dust-free optical setup with anti-reflective coatings on lenses and gratings are useful to reduce unwanted random Gaussian noise and ring-like noise from back reflections. The laser beam source can be expanded to a larger beam than the object of interest to produce a more uniform light source, particularly since the laser has considerably more power than necessary. In future, the influence of the quarter wave plates can be reduced by using the four-image solution suggested by Ajovalasit et al. [9]. The small field of view in this setup lends itself to relatively coarse image resolution over the long distances between the object and the CCD, so larger fields of view may allow for better image resolution. Also, use of larger diameter lenses, particularly for the first and

last lenses, and image distortion-corrected lenses should also improve the image resolution.

Potential Applications

This new approach to simultaneous acquisition of phase-stepped photoelastic images has potential for many applications where phase stepping cannot be achieved sequentially. Prior stress analysis for diametric compression of a disk utilizes a stress-frozen disk. Here we obtained the image in Fig. 2(a) from a 10-μs exposure during active loading of the disk at a displacement rate of 4 μm/s. Sequential phase-stepping and image capture could not achieve the fast rotations of the optics and image acquisition rates required to produce quality data for even this slow quasi-static loading. The same is true for the compressed plate with a hole which was loaded at a constant displacement rate of 8 μm/s. The rate was slow enough for image acquisition with a standard CCD with exposures of 10 μs, allowing for the same experimental setup as used above for the compressed disk.

Our technique is highly configurable, allowing for a myriad of laser light sources, field of view sizes, and cameras. Though the design of the initial setup does require Fourier analysis, the resulting configuration can easily be altered through minor changes to the inputs to the analysis. Although all of the components used in this study are commercially available, the setup would benefit from custom design and fabrication of the diffraction grating. A custom 2D transmission diffraction grating would improve system performance by reducing back reflections in the system and by increasing the intensity of each individual phase-stepped beam, which could be important for high-rate imaging. Given the slow acquisition rate required, the laser and two 1D gratings used in this study were more than sufficient to provide enough light. The laser light before the specimen was only 200 μW over the 12-mm beam and 13 μW for the ($\pm 1, \pm 1$) beams. Also, the laser in this setup allows for larger beam expansion, given the minimal power requirement for image acquisition. The current configuration has a limited range of field of view and image acquisition rate, but this technique could easily be extended to larger fields of view and faster frame rates for dynamic events.

To demonstrate the flexibility of this technique for a dynamic experiment, we describe the design for a high-speed camera viewing a 50-mm diameter disk. The camera specifications are for a Photron FASTCAM SA3, which has a 1024 pixel × 1024 pixel sensor with 17 μm × 17 μm pixel size, meaning a 17.41 mm × 17.41 mm sensor, at 1000 fps. To fit four images of 50-mm object on this sensor without overlap, we assume the desired magnification, M, is −0.16, an image to object height ratio of −8 mm / 50 mm, and an object length to pixel ratio of 106 μm/pixel. Here, we assume that a 532-nm wavelength laser beam can

be expanded to a collimated diameter larger than the 50-mm diameter disk. For this magnification, a 54-mm × 54-mm object area will not overlap on the sensor, which can be achieved either by limiting the collimated laser beam diameter or by using an aperture to reduce the visible area. It is advantageous to use 1-inch diameter optics when the beams are split to reduce the amount of beam separation required for the arrays of four lenses and mirrors in the setup, but this implies that the system must be designed so that the split beams must be small enough to transmit through or reflect off of these optics.

From a Fourier analysis described in the Appendix, we determined that one feasible configuration of optics has the following features. The lens focal lengths, f_1 through f_5 are 250 mm, 50 mm, 150 mm, 100 mm, and 100 mm. The first lens should have a 3-inch diameter in order to accommodate the large diameter laser beam immediately after the sample, but beams are subsequently reduced in size in this configuration so that the other lenses can have 1-inch diameters. The 2D transmission diffraction gratings have pitch p of (1/250) mm (4.0 μm). The resulting first-order diffraction angle κ for 532-nm light is 0.133 radians (7.64^o). To center the four images at (± 4.35 mm, ± 4.35 mm) on the sensor with a 100-mm final lens, the angle β of the beams after the second set of redirecting mirrors is 0.0435 radians (2.49^o). The nominal distances d_a through d_k are listed without considering the thickness of each lens: 50 mm, 100 mm, 200 mm, 99 mm, 203 mm, 150 mm, 147 mm, 43 mm, 150 mm, 391 mm, and 100 mm. The arrays of optics have the following ($\pm x, \pm y$) distance from the center of each optic to the (0,0) centerline, based on the angles κ and β: f_3 lenses at 27 mm, analyzing optics at 47 mm, first set of redirecting mirrors at 66.5 mm, second set of redirecting mirrors at 23.5 mm, and f_4 lenses at 17 mm. The final lens is located where all four beams cross the (0,0) centerline. For this set of optics, translations of the f_3 and f_4 lens arrays, without translation of any other optics other than possibly the analyzing optics, allows for magnifications from −0.37 down to −0.11, meaning object length to pixel ratio of 46 μm/pixel to 155 μm/pixel, or object area of 24 mm × 24 mm to 79 mm × 79 mm, respectively. This example shows how this design approach can be employed for high speed cameras to capture dynamic photoelastic events.

Conclusions

We have presented a new approach to simultaneous image acquisition of phase-stepped photoelastic patterns with a single camera by using diffraction gratings. We described the design process for the setup and indicated the important design variables that affect the final field of view size.

This technique results in full-field isoclinic and isochromatic data for cases where sequential phase-stepping is not possible, as demonstrated by the quasi-static diametric compression of a Homalite-100 disk and quasi-static compression of a Homalite-100 plate with a central hole. We provided two examples of experimental setups, one setup used for the two experiments described here and one hypothetical setup designed for a high-speed camera application. We also characterized several potential error sources in the technique so that users can design their experimental setups as to minimize these errors. By using monochromatic laser light that comes in a wide range of powers and an imaging method that is not tied to a single type of camera, this technique is adaptable to many configurations, from small to large fields of view, to study static to dynamic events.

Appendix

We conducted two types of Fourier wave-optics analysis to determine the focal length of each lens and the distance between each optic. The first is using the ideal Fourier representation of thin lenses, and the second is using the Fourier representation of thick lenses, accounting for the refractive index of the lens material for a given wavelength and curvatures. The first analysis is useful for determining approximate values for purchase of optics based on a desired magnification on the camera; this simpler analysis is provided below. The second analysis is for a specific system, and thus contains more variables than is appropriate for this paper. The reader is referred to [15] for further information on this type of analysis.

The Fourier wave-optics analysis begins with the matrix representations of coherent light, thin lenses, and propagation through free space. The matrix for coherent light at any point in space is a 2×1 vector with the length L from the propagation axis and angle of propagation ϕ relative to the propagation axis, written as

$$\mathfrak{C}\{L, \phi\} = \begin{bmatrix} L \\ \phi \end{bmatrix}. \tag{4}$$

The 2×2 matrix representation of a lens includes the focal length f, given by

$$\mathfrak{L}\{f\} = \begin{bmatrix} 1 & 0 \\ -\frac{1}{f} & 1 \end{bmatrix}. \tag{5}$$

The 2×2 matrix representation of light propagating a distance D in free space is given by

$$\mathfrak{F}\{d\} = \begin{bmatrix} 1 & d \\ 0 & 1 \end{bmatrix}. \tag{6}$$

Coherent light originating at an object plane is considered "in focus" at the image plane when the length component, L_I does not depend on the angular component of the light at the object plane, ϕ_O, after propagating through the optical system. The magnification of the object at the image plane, denoted M, is defined by L_I/L_O.

The analysis of the proposed system will only include the five lenses and propagation in space. The user has discretion on how to place the other optics in order to achieve the desired beam propagation and field of view. Let the distances in the system shown in Fig. 1 be represented as distance between lenses, such that $D_O = d_a$, $D_1 = d_b + d_c$, $D_2 = d_d + d_e$, $D_3 = d_f + d_g + d_h + d_i$, $D_4 = d_j$, and $D_5 = d_k$. In general, the light at the image plane is represented by

$$\begin{aligned} \mathfrak{C}_I\{L_I, \phi_I\} =& \mathfrak{F}\{D_5\} \cdot \mathfrak{L}\{f_5\} \cdot \mathfrak{F}\{D_4\} \cdot \mathfrak{L}\{f_4\} \\ & \cdot \mathfrak{F}\{D_3\} \cdot \mathfrak{L}\{f_3\} \cdot \mathfrak{F}\{D_2\} \cdot \mathfrak{L}\{f_2\} \\ & \cdot \mathfrak{F}\{D_1\} \cdot \mathfrak{L}\{f_1\} \cdot \mathfrak{F}\{D_O\} \\ & \cdot \mathfrak{C}_O\{L_O, \phi_O\}. \end{aligned} \tag{7}$$

As described above, the last lens is placed a distance equal to its focal length ($D_5 = f_5$), and the first two lenses are placed a distance equal to the sum of their focal length apart ($D_1 = f_1 + f_2$), and therefore,

$$\begin{aligned} \mathfrak{C}_I\{L_I, \phi_I\} =& \mathfrak{F}\{f_5\} \cdot \mathfrak{L}\{f_5\} \cdot \mathfrak{F}\{D_4\} \cdot \mathfrak{L}\{f_4\} \\ & \cdot \mathfrak{F}\{D_3\} \cdot \mathfrak{L}\{f_3\} \cdot \mathfrak{F}\{D_2\} \cdot \mathfrak{L}\{f_2\} \\ & \cdot \mathfrak{F}\{f_1 + f_2\} \cdot \mathfrak{L}\{f_1\} \cdot \mathfrak{F}\{D_O\} \\ & \cdot \mathfrak{C}_O\{L_O, \phi_O\}. \end{aligned} \tag{8}$$

The coefficient in front of L_O term in L_I of equation (8) is $(-D_3 + f_3 + f_4) * (f_2 f_5/(f_1 f_3 f_4))$; also, this coefficient is equal to M. Therefore, solving for D_3 gives

$$D_3 = f_3 + f_4 - \frac{f_1 f_3 f_4}{f_2 f_5} M. \tag{9}$$

The distance D_3 only depends on the focal lengths of the lenses and the desired magnification. Since the coefficient in front of ϕ_O in L_I must be equal to zero for the image to be in focus, then substituting equation (9) into (8) results in the following equation:

$$\frac{f_1 f_3 f_5}{f_2 f_4} + \left(D_O - f_1 + \frac{D_2 f_1^2}{f_2^2} - \frac{f_1^2}{f_2} - \frac{f_1^2 f_3}{f_2^2} \right) M = 0. \tag{10}$$

Solving for D_2 gives

$$D_2 = f_2 + f_3 - \frac{(D_O - f_1)f_2^2}{f_1^2} - \frac{f_2 f_3 f_5}{f_1 f_4 M}. \tag{11}$$

The distance D_2 depends on the focal lengths of the lenses, the desired magnification, and the distance between the object and the first lens. Substituting both equations (9) and (11) into equation (8) results in $L_I = M L_O$, implying that the image is in focus regardless of distance D_4.

References

1. Patterson EA, Wang ZF (1998) Simultaneous observation of phase-stepped images for automated photoelasticity. J Strain Anal 33(1):1–15
2. Barone S, Burriesci G, Petrucci G (2002) Computer aided photoelasticity by an optimum phase stepping method. Exp Mech 42(2):132–139
3. Ramesh K (2000) Digital photoelsticity. Springer, New York
4. Yoneyama S, Kikuta H (2006) Phase-stepping photoelasticity by use of retarders with arbitrary retardation. Exp Mech 46(3):289–296
5. Yoneyama S, Kikuta H, Moriwaki K (2006) Simultaneous observation of phase-stepped photoelastic fringes using a pixelated microretarder array. Opt Engr 45(8):083604–1–083604–7
6. Kramer SLB, Mello M, Ravichandran G, Bhattacharya K (2009) Phase-shifting full-field interferometric methods for determination of in-plane tensorial stress. Exp Mech 49(2):303–315
7. Hobbs JW, Greene RJ, Patterson EA (2003) A novel instrument for transient photoelasticity. Exp Mech 43(4):403–409
8. Zhu B, Ueda K (2003) Real-time wavefront measurement based on diffraction grating holography. Opt Comm 225(1–3):1–6
9. Ajovalasit A, Barone S, Petrucci G, Zuccarello B (2002) The influence of the quarter wave plates in automated photoelasticity. Opt Lasers Engr 38(1–2):31–56
10. Tippur HV, Krishnaswamy S, Rosakis AJ (1991) A coherent gradient sensor for crack tip deformation measurements: analysis and experimental results. Int J Fract 48(3):193–204
11. Siegmann P, Backman D, Patterson EA (2005) A robust approach to demodulating and unwrapping phase-stepped photoelastic data. Exp Mech 45(3):278–289
12. Timoshenko S, Goodier JN (1951) Theory of elasticity, 2nd edn. McGraw-Hill Book Co. Inc., New York
13. Ramesh K, Kaslmayan T, Neethi Simon B (2011) Digital photoelasticity - a comprehensive review. J Strain Anal 46(4):245–266
14. Prashant PL, Ramesh K (2006) Genesis of various optical arrangements of circular polariscope in digital photoelsticity. J Aerosp Sci Technol 58(2):117–132
15. Goodman JW (2004) Introduction to fourier optics, 3rd edn. Roberts and Company Publishers, Greenwood Village